

Simultaneous Performance and Stability Improvement of Ternary Polymer Solar Cells Enabled by Modulating the Molecular Packing of Acceptors

Huimin Gu, Lingpeng Yan, Zerui Li, Jianqi Zhang, Qun Luo, Yongzhen Yang,*
Xuguang Liu, Zhixiang Wei,* and Chang-Qi Ma*

Nanoscale morphology of the active layer plays a crucial role in the power conversion efficiency (PCE) and stability of polymer solar cells (PSCs). Blending the photoactive layer with a third component to produce a ternary system is considered a reliable approach to tune the nanomorphology, thereby improving the device performance. Herein, poly[(2,6-(4,8-bis(5-(2-ethylhexyl)thiophen-2-yl)benzo[1,2-*b*:4,5-*b'*]-dithiophene)-co-(1,3-di(5-thiophen-2-yl)-5,7-bis(2-ethylhexyl)benzo[1',2'-*c*:4,5-*c'*]-dithiophene-4,8-dione))] (PBDB-T): 3,9-bis(2-methylene-(3-(1,1-dicyanomethylene)-indanone))-5,5,11,11-tetrakis(4-hexylphenyl)-dithieno[2,3-*d*:2',3'-*d'*]-s-indaceno[1,2-*b*:5,6-*b'*]-dithiophene (ITIC) solar cells doped with a third small molecule are systematically investigated, namely, (5Z,5'Z)-5,5'-((7,7'-(9,9-dioctyl-9H-fluorene-2,7-diyl)bis(benzo[*c*]1,2,5]thiadiazole-7,4-diyl))-bis(methanylylidene))bis(3-ethyl-2-thioxothiazolidin-4-one) (FBR). Owing to the wide optical bandgap of FBR, blending PBDB-T:ITIC with FBR increases the device's light-harvesting capability in the short wavelength range (400–550 nm), which improves the short circuit current. Differential scanning calorimetry and grazing incidence wide angle X-ray scattering analyses reveal that the FBR exhibits impressive miscibility with ITIC, leading to the formation of ITIC:FBR alloys. Optimum performance is achieved with a PBDB-T:ITIC:FBR (1:0.8:0.2) cell, which yields a PCE of 11.17%, demonstrating a 10% improvement relative to the PBDB-T:ITIC binary cell. Crucially, the ternary solar cells also show improved device stability, which is attributed to the formation of ITIC:FBR alloys suppressing the crystallization of ITIC. This study provides deep insights into the performance- and stability-related improvements available to PSCs devices that incorporate a third conjugated small molecule.

1. Introduction

Organic solar cells (OSCs) have garnered considerable scientific attention in recent years owing to their lightweight, low cost, and large-area printing compatibility, making them promising candidates for building integrated applications.^[1a–d] Since the first report of high-performance, the acceptor–donor–acceptor (A-D-A)-type non-fullerene acceptor (NFA) 3,9-bis(2-methylene-(3-(1,1-dicyanomethylene)-indanone))-5,5,11,11-tetrakis(4-hexylphenyl)-dithieno[2,3-*d*:2',3'-*d'*]-s-indaceno[1,2-*b*:5,6-*b'*]-dithiophene (ITIC),^[2] various A-D-A-type NFAs have been developed, in some cases achieving a high power conversion efficiency (PCE) of more than 18%.^[3] In comparison with fullerene acceptors, NFAs offer several advantages, including high light absorption ability, ease of structure and optical property modification, and potential for large-scale synthesis, and have been considered as the most promising materials in polymer solar cells.^[4a–c]


Of the NFAs investigated to date, ITIC is the most representative. By blending ITIC with the wide bandgap polymer poly[(2,6-(4,8-bis(5-(2-ethylhexyl)thiophen-2-yl)

H. Gu, Dr. L. Yan, Z. Li, Prof. Q. Luo, Prof. C.-Q. Ma
Printable Electronics Research Center
Suzhou Institute of Nano-Tech and Nano-Bionic
Chinese Academy of Sciences (CAS)
Suzhou 215123, P. R. China
E-mail: cqma2011@sinano.ac.cn

H. Gu, Dr. L. Yan, Prof. Y. Yang, Prof. X. Liu
Key Laboratory of Interface Science and Engineering in Advanced Materials
Ministry of Education
Taiyuan University of Technology
Taiyuan 030024, P. R. China
E-mail: yyzyut@126.com

Dr. L. Yan
Institute of New Carbon Materials
Taiyuan University of Technology
79 Yingze Street, Taiyuan 030024, P. R. China

Dr. J. Zhang, Prof. Z. Wei
CAS Key Laboratory of Nanosystem and Hierarchical Fabrication
CAS Center for Excellence in Nanoscience
National Center for Nanoscience and Technology
Beijing 100190, P. R. China
E-mail: weizx@nanoctr.cn

 The ORCID identification number(s) for the author(s) of this article can be found under <https://doi.org/10.1002/solr.202000374>.

DOI: 10.1002/solr.202000374

benzo[1,2-*b*:4,5-*b'*]-dithiophene)-co-(1,3-di(5-thiophen-2-yl)-5,7-bis(2-ethylhexyl)benzo[1',2'-*c*:4,5-*c'*]dithiophene-4,8-dione)] (PBDB-T), a polymer solar cell with a high PCE of 11.3% has been realized.^[5] Further structural modification of ITIC using terminal F atoms (3,9-bis(2-methylene-((3-(1,1-dicyanomethylene)-6,7-difluoro-*o*)indanonone))-5,5,11,11-tetrakis(4-hexylphenyl)-dithieno[2,3-*d*:2',3'-*d'*]-*s*-indaceno[1,2-*b*:5,6-*b'*]dithiophene, IT-4F)^[6] or methyl groups (3,9-bis(2-methylene-((3-(1,1-dicyanomethylene)-6/7-methyl)indanonone))-5,5,11,11-tetrakis(4-hexylphenyl)-dithieno[2,3-*d*:2',3'-*d'*]-*s*-indaceno[1,2-*b*:5,6-*b'*]dithiophene, IT-M)^[7] has produced polymer solar cells with a PCE exceeding 13% when used in combination with the modified polymer donor, PBDB-T-2F. In addition, when ITIC was blended with a second low-bandgap acceptor, named ternary solar cells, such as IT-4F,^[8] 2,2'-((2Z,2'Z)-(((4,4,9,9-tetrakis(4-hexylphenyl)-4,9-dihydro-*s*-indaceno[1,2-*b*:5,6-*b'*]-dithiophene-2,7-diyl)bis(4-((2-ethylhexyl)oxy)thiophene-5,2-diyl))bis(methanylylidene))bis(5,6-difluoro-3-oxo-2,3-dihydro-1H-indene-2,1-diylidene))dimalononitrile (IEICO-4F),^[9] or poly([N,N0-bis(2-octylododecyl)-naphthalene-1,4,5,8-bis(dicarboximide)-2,6-diyl)-alt-5,5'-(2,2'-bithiophene)] (N2200),^[10] further PCE improvements were achieved owing to the increase in the short circuit current (J_{sc}) originating from the broader light-harvesting capability in the near-IR (NIR) region. On the other hand, the use of wide bandgap electron acceptors is also considered to be an effective method to improve the performance of solar cells, as such a ternary strategy would increase the light absorption ability at short wavelengths and the V_{oc} of the cell owing to its high-lying lowest unoccupied molecular orbital (LUMO) energy level. In general, this ternary blending strategy facilitates the formation of an alloy-like morphology. For example, Chen et al. used two small NFA molecules, TPE-4PDI and FT-2PDI, respectively, to form an alloy-like morphology with 3,9-bis(2-methylene-(3-(1,1-dicyanomethylene)-indanonone))-5,5,11,11-tetrakis(5-hexylthienyl)-dithieno[2,3-*d*:2',3'-*d'*]-*s*-indaceno[1,2-*b*:5,6-*b'*]dithiophene and to regulate the increase in the V_{oc} of the device.^[11] Alternatively, Ma et al. used MeIC and BTP-4F-12 to form an alloy-like morphology, which reduced the energy loss in the device, thereby regulating the increase in the V_{oc} of the device while also improving its performance.^[12] In addition, the alloy-like morphology utilized by An et al. comprised MF1 and Y6 and increased the photon absorption capacity and charge mobility of the device, achieving a photoelectric conversion performance of 17.22%.^[13] Despite these efforts, ternary blending strategies remain relatively unexplored.

As for the PBDB-T:ITIC solar cell, owing to the insufficient light-harvesting capability of both the PBDB-T polymer and the ITIC acceptor in the wavelength range of 400–600 nm, low external quantum efficiency (EQE) over the 400–600 nm range was measured for the binary cell.^[9,10] To solve this problem, fullerene derivatives, including [6,6]-phenyl- C_{71} -butyric acid methyl ester (PC₇₁BM)^[14a-d] and 1',1'',4',4''-tetrahydro-di[1,4]methanonaphthaleno[5,6]fullerene- C_{60} (ICBA),^[14] were used as the third component in the PBDB-T:ITIC blends to improve the light-harvesting performance over the 400–600 nm range. Nonetheless, owing to the low light absorption ability of fullerene molecules and synthesis-related difficulties, fullerene derivatives are not ideal for this purpose. Therefore, the identification of a third conjugated molecule with short-wavelength absorption is of great

significance for improving the performance of polymer solar cells as well as developing a multi-component blend system for their fabrication. Very recently, polymer dispersity index (PDI) derivatives^[15] and wide bandgap acceptor small molecules^[16] were also used as the third component to improve device performance, yielding a PCE of $\approx 11.5\%$ for the PBDB-T:ITIC-based ternary cell.

After efficiency, stability is the next critical issue currently limiting the commercialization of polymer solar cells. Despite the aforementioned research into improving the PCE of these ternary cells, reports considering the operation stability of PBDB-T:ITIC-based ternary solar cells are rather limited.^[17a,b] In this work, a wide bandgap A-D-A-type small molecule (5Z,5'Z)-5,5'-((7,7'-(9,9-dioctyl-9H-fluorene-2,7-diyl)bis(benzo[c]1,2,5)thiadiazole-7,4-diyl))-bis(methanylylidene))bis(3-ethyl-2-thioxothiazolidin-4-one) (FBR), which exhibits strong absorption in the short wavelength band (450–600 nm) and is inexpensive owing to the ease of synthesis, is introduced as the second electron acceptor in the PBDB-T:ITIC binary blend system. Experiment results confirm that blending the PBDB-T:ITIC with FBR improves device performance and stability simultaneously. Systematic investigation of the intermolecular interaction between FBR and ITIC confirms that FBR is able to modulate the nano-crystal structure of ITIC, thus representing a promising mechanism by which the performance and stability of the ternary solar cell can be improved.

2. Results and Discussions

2.1. Photophysical Properties of the Three Compounds

The chemical structures of PBDB-T, ITIC, and FBR as well as the device structure investigated in the study are shown in **Figure 1a**. To understand the interaction between these three components, we first checked their light absorption properties. **Figure 1b** shows the UV-vis absorption spectra of the three compounds in the thin solid film. The absorption maxima of PBDB-T, ITIC, and FBR are situated at 627, 648, and 519 nm, respectively, and the corresponding optical bandgaps are estimated to be 1.80, 1.54, and 2.06 eV, respectively, from the absorption onset wavelength. Clearly, by covering the entirety of the visible wavelength range, the absorption spectrum of FBR complements the PBDB-T:ITIC components. **Figure 1c** shows the absorption spectra of the ternary blend films with different ITIC:FBR blend ratios (keeping a constant donor:acceptor ratio of 1:1, w/w). It is observed that, with the increase in the FBR blending ratio, the absorption band of FBR (over 300–600 nm) increases gradually, whereas that of ITIC (650–760 nm) decreases. Crucially, a redshift of the ITIC maximum absorption peak is observed upon the addition of FBR, indicating the intensive intermolecular interaction between ITIC and FBR, which is ascribed to the formation of an ITIC:FBR alloy in this blend film as confirmed by the grazing incidence wide angle X-ray scattering (GIWAXS) and differential scanning calorimeter (DSC) results (*vide infra*). Nevertheless, upon FBR doping, intensive light absorption over 300–750 nm can be achieved for the ternary film, which would increase the light-harvesting capability of the solar cells.

To reveal the interaction between ITIC and FBR, photoluminescence (PL) spectra were measured for ITIC:FBR films with

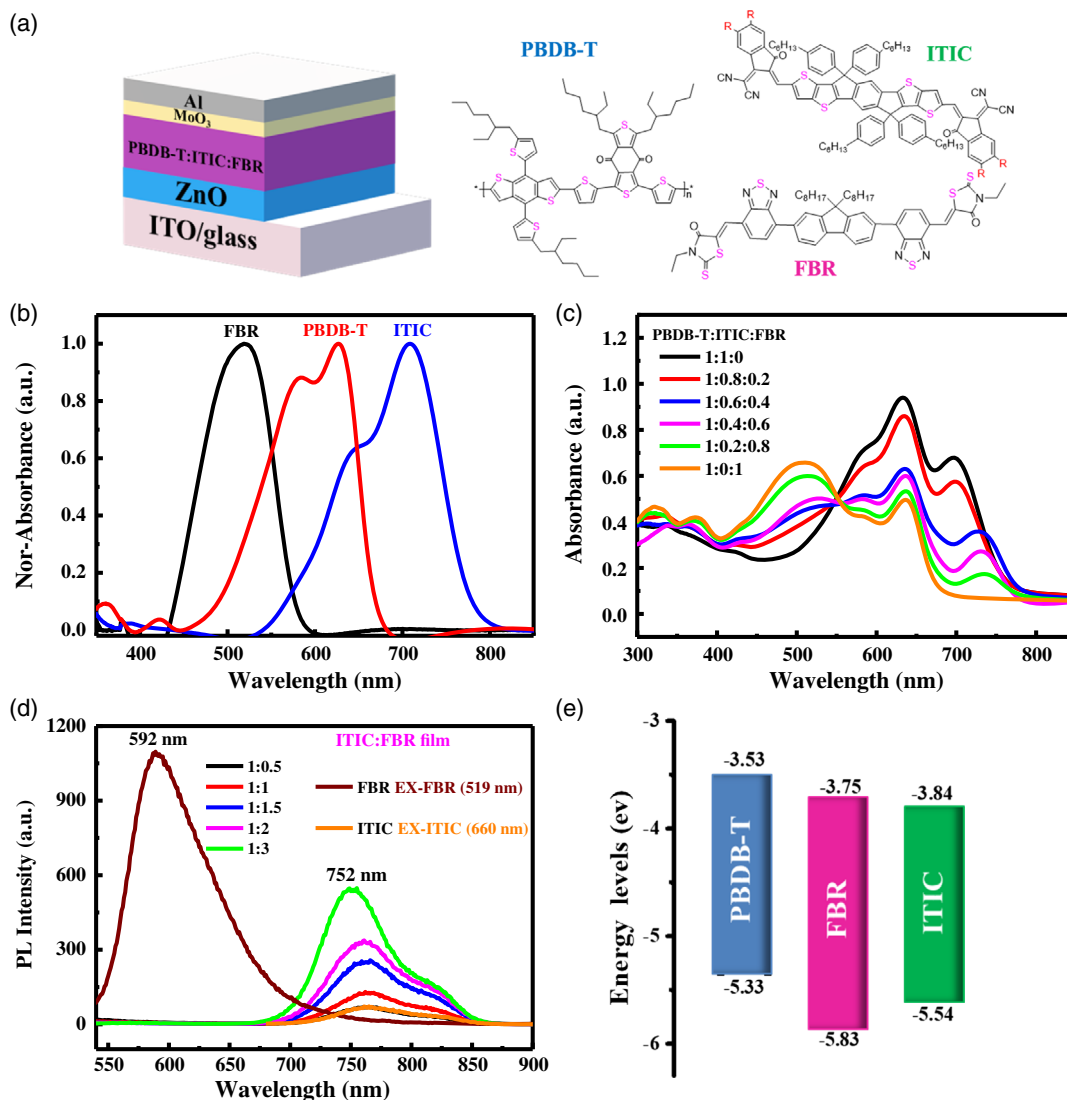


Figure 1. a) Structure of the ternary devices and the chemical structures of PBDB-T, ITIC, and FBR. b) Normalized UV-vis absorption spectra of PBDB-T, ITIC, and FBR films. c) UV-vis spectra of PBDB-T:ITIC:FBR films with different ITIC:FBR blend ratios. d) PL spectra of FBR:ITIC films excited at 519 nm and ITIC film excited at 660 nm. e) Energy level alignment of PBDB-T, ITIC^[18a] and FBR.^[18b]

different ratios (see Figure 1d). It is observed that the neat FBR film shows a broad PL spectrum peaking at 592 nm, which overlaps comfortably with the absorption spectra of PBDB-T and ITIC. When blended with ITIC, the resultant FBR:ITIC blend film shows only the emission of ITIC peaking at 752 nm,^[16] suggesting very efficient intermolecular energy transfer from FBR to ITIC. Meanwhile, almost no FBR fluorescence can be detected for the blend ratios of 1:0.5–1:3, suggesting that these two components are thoroughly intermixed, with no phase separation (over 10 nm) detected. Moreover, this phenomenon also exists in ternary blended films (Figure S1, Supporting Information). However, this energy transfer phenomenon does not exist when ITIC is excited at 660 nm (Figure S2, Supporting Information). The energy levels of PBDB-T, ITIC, and FBR are cited from the literature, and the energy alignment is shown in Figure 1e.^[18a,b] This reveals that the LUMO of PBDB-T is -3.53 eV, which is

higher than that of FBR (-3.75 eV) and ITIC (-3.84 eV), whereas the highest occupied molecular orbital (HOMO) level of PBDB-T is -5.33 eV, which is higher than that of FBR (-5.83 eV) and ITIC (-5.54 eV). Such an energy alignment facilitates the photon-induced charge transfer from PBDB-T (electron donor) to ITIC and FBR (electron acceptors), which is supported by the PL quenching by either acceptor.

2.2. Thermodynamic Behaviors of PBDB-T:FBR:ITIC Films

To elucidate the interaction between the three components, DSC measurements were performed to investigate the thermal behavior of the blends. To simulate the interaction of these three molecules in the thin solid film of solar cell, the samples for DSC measurement were prepared by casting the solution of these materials. Figure 2 shows the DSC curves of PBDB-T:ITIC:

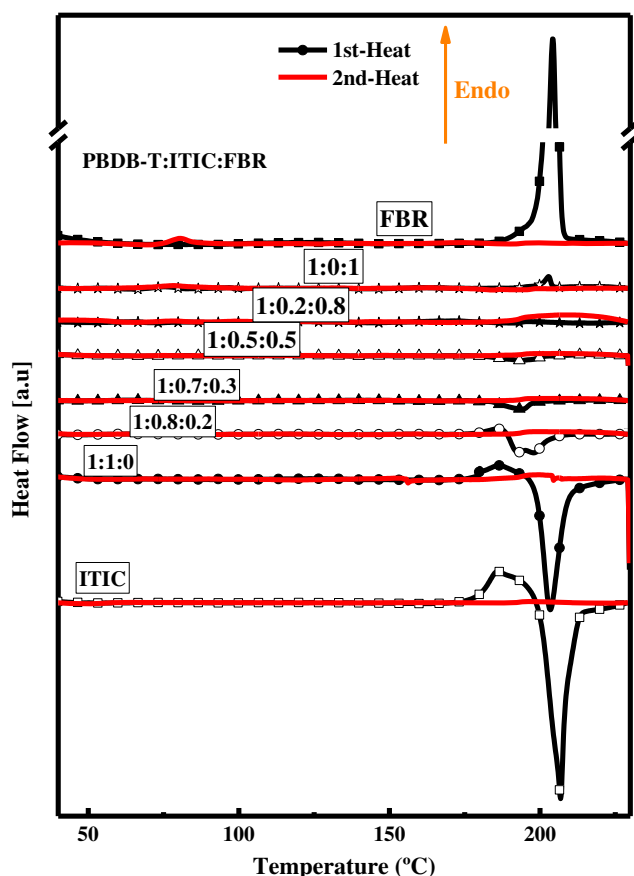


Figure 2. DSC curves of ternary blend films with different FBR ratios.

FBR films at a scan rate of $10\text{ }^{\circ}\text{C min}^{-1}$ in comparison with the curves of pure ITIC and FBR under nitrogen. For comparison, the DSC curves of PBDB-T are shown in Figure S3, Supporting Information, demonstrating that no obvious phase transition was measured for the PBDB-T polymer over the $40\text{--}250\text{ }^{\circ}\text{C}$ temperature range. As shown in Figure 2, FBR shows a clear melting point with a peaking temperature at $204\text{ }^{\circ}\text{C}$, with this feature also observed for the PBDB-T:FBR blend. However, this FBR melting peak was absent in all measurements of the PBDB-T:ITIC:FBR ternary blend films, even for the blend containing an FBR content of 80%, indicating that, owing to the presence of ITIC, FBR is thoroughly mixed into the ternary blend films. On the other hand, both ITIC and the PBDB-T:ITIC (1:1) binary blend show a broad endothermic process starting at $174\text{ }^{\circ}\text{C}$, which is followed by a sharp exothermic process peaking at $206\text{ }^{\circ}\text{C}$. This abnormal phenomenon was also reported by Yu et al., and these two processes are ascribed to the polymorph phase transition (melting of the nanocrystals) and the long-range diffusion crystallization of ITIC.^[19] In the ternary blend system of PBDB-T:ITIC:FBR containing 20% FBR, the melting endotherm (starting at $186\text{ }^{\circ}\text{C}$) and the crystallization (peaking at $199\text{ }^{\circ}\text{C}$) of ITIC nanocrystals are still prominent but with slightly lower enthalpy. This indicates that ITIC nanocrystals persist in this ternary blend system. In addition to these, an exotherm process at $193\text{ }^{\circ}\text{C}$ was measured for the ternary films containing a low proportion of FBR dopant

($20\text{--}40\%$), confirming the formation of new crystalline phases in the ternary blend. It is noted that the polymorph transition of ITIC nanocrystals disappears with an increase in the FBR blending concentration, leaving a single exotherm at $193\text{ }^{\circ}\text{C}$; therefore, it can be inferred that ITIC:FBR alloy nanocrystals are formed during this exotherm process, with this hypothesis receiving further support from the GIWAXS results (*vide infra*). In addition, it can be observed that increasing the doping ratio of FBR further ($>50\%$) causes the disappearance of the exotherm at $193\text{ }^{\circ}\text{C}$, indicating that excessive FBR doping is not conducive to the formation of ITIC:FBR alloy nanocrystals. In summary, a small amount of FBR ($<50\%$) promotes the formation alloy nanocrystals to maintain morphological stability, whereas increasing the amount of FBR doping further has an adverse effect.

2.3. Morphology of Blend Films

To understand the intermolecular interaction and molecular packing alignment within the blend films in greater detail, the morphologies of PBDB-T, ITIC, FBR, PBDB-T:ITIC (1:1), PBDB-T:ITIC:FBR (1:0.8:0.2), and PBDB-T:FBR (1:1) films were measured by GIWAXS and atomic force microscopy (AFM). Figure 3a–f shows the 2D-GIWAXS patterns of the films comprising these three compounds in various blend ratios. The corresponding diffraction profiles along the out-of-plane (OOP) and in-plane (IP) directions are shown in Figure 3g. The pristine PBDB-T exhibits OOP (100) and (010) diffraction, indicating that the $\pi\text{--}\pi$ stacking is oriented in a face-on mode along the q_z axis at 0.29 \AA^{-1} (corresponding to a d spacing of 21.7 \AA) and 1.72 \AA^{-1} (corresponding to a d spacing of 3.65 \AA)—these results are in close accordance with the literature.^[20] The pristine ITIC film shows strong symmetric ordering of its lamellae. This interpretation is based on a peak position ratio of 1:3 relative to the primary OOP peaks at $q_z \cong 0.51\text{ \AA}^{-1}$ (corresponding to a d spacing of 12.3 \AA) and 1.61 \AA^{-1} (corresponding to a d spacing of 3.90 \AA) (Figure 3c,g), as well as the $\pi\text{--}\pi$ stacking in the face-on mode along the q_z axis at $q_z \cong 1.61\text{ \AA}^{-1}$.^[17a,21] By contrast, the pristine FBR film does not show significant $\pi\text{--}\pi$ stacking oriented in the OOP direction. When these materials form a blended film, the molecular orientation within the film changes greatly. Nevertheless, strong $\pi\text{--}\pi$ stacking diffraction is discernible; the characteristic PBDB-T and ITIC lamellae ordering is present in the PBDB-T:ITIC binary film, indicating good miscibility between PBDB-T and ITIC (Figure 3b). In addition, by comparing the (010) OOP scattering peak of the ITIC film (Figure 3b) to that of the PBDB-T:ITIC film (Figure 3d), an ITIC (010) OOP scattering peak is also present at 1.61 \AA^{-1} , demonstrating the formation of ITIC nanocrystals within PBDB-T:ITIC blend films. The coherence lengths (L_c) of PBDB-T and ITIC in each film were calculated according to Equation (2)

$$L_c = 2\pi k / f_{\text{whm}} \quad (1)$$

where k is the shape factor, typically with a value of 0.9, and f_{whm} denotes the full width at half maximum of the diffraction peak. The coherence lengths L_c associated with the $\pi\text{--}\pi$ stacking in the PBDB-T:ITIC and PBDB-T:ITIC:FBR systems were calculated as 1.38 and 2.57 nm, respectively. The increased L_c in the ternary

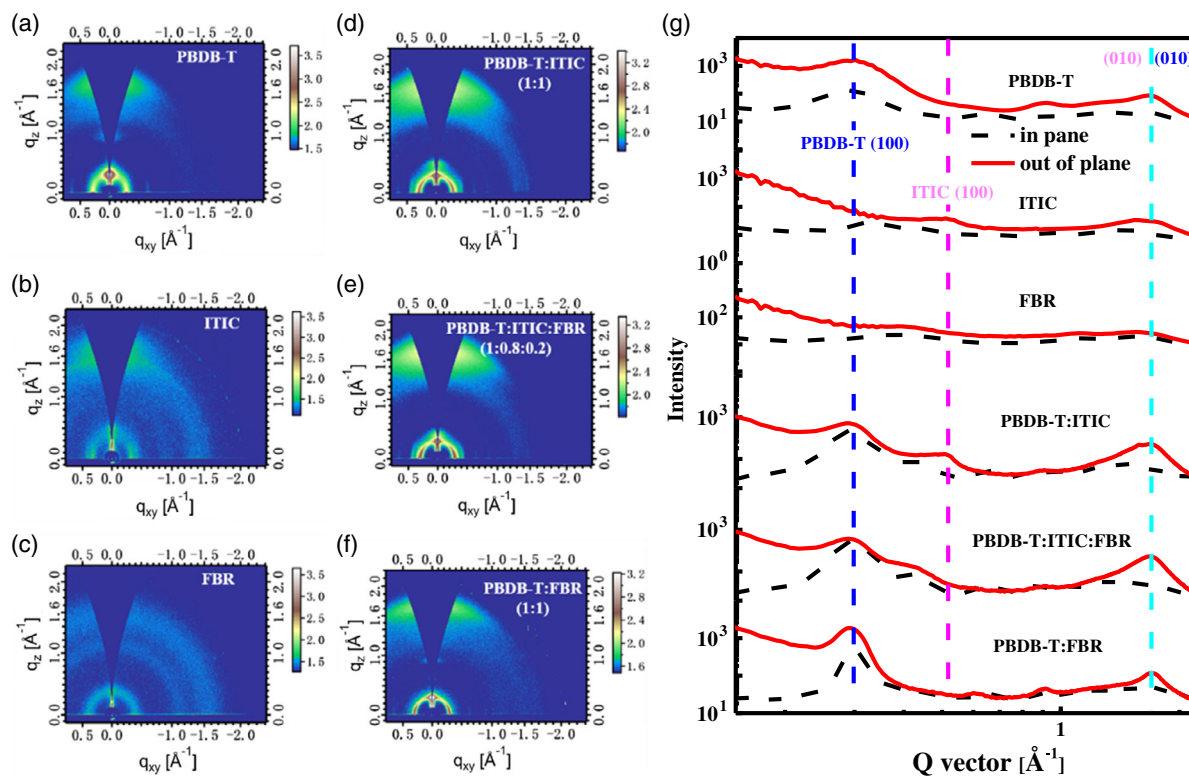


Figure 3. 2D-GIWAXS images of a) PBDB-T, b) PBDB-T:ITIC (1:1), c) ITIC, d) PBDB-T:ITIC:FBR (1:0.8:0.2), e) FBR, and f) PBDB-T:FBR (1:1). g) GIWAXS intensity profiles along the IP (dotted line) and OOP (solid line) directions.

blend corresponds to the higher crystallinity in the heterojunction domain, indicating better phase separation. This is favorable for promoting photogenerated charge dissociation and transport. These results are consistent with increased J_{sc} and improved device performance.

For the PBDB-T:FBR film, in addition to the (100) diffraction peak at 0.29 \AA^{-1} for PBDB-T, the (200) and (300) diffraction peaks of PBDB-T were also measured. No scattering peaks due to FBR can be found, indicating that FBR is thoroughly incorporated into the PBDB-T crystalline matrix. However, blending the PBDB-T:ITIC film with 20% FBR increases the scattering intensity at 1.72 \AA^{-1} , which is supposedly due to the formation of ITIC:FBR alloys. Nevertheless, these results indicate that FBR has a certain regulating effect on the degree of crystallization of PBDB-T and/or ITIC,^[22] thus corroborating the DSC results.

Furthermore, the surface morphologies of PBDB-T:ITIC binary and PBDB-T:ITIC:FBR ternary blends were analyzed using AFM, as shown in **Figure 4a–c**. All the blend films present uniform and well distributed film morphologies with a root-mean-square (RMS) roughness of less than 2 nm, indicating good miscibility among blend components. The PBDB-T:ITIC:FBR ternary film shows a slightly higher RMS of 2.07 nm as compared with 1.91 nm for the pure PBDB-T:ITIC binary system. Moreover, as shown in the transmission electron microscopy (TEM) images (**Figure 4d–f**) of the three blended films, the PBDB-T:ITIC:FBR ternary film shows finer structure, suggesting a good compatibility of its three constituent components. The well-formed morphologies and phase

separation are beneficial to facilitate charge dissociation and reduce charge recombination, and are consistent with the GIWAXS results.

Considering that the introduction of FBR may also increase the electron mobility within the active layer, potentially another reason for the improved device performance, the electron mobility of active layers based on three structures (PBDB-T:ITIC, PBDB-T:ITIC:FBR (1:0.8:0.2), and PBDB-T:FBR) was tested, with the experimental results shown in **Figure S4** and **Table S1**, Supporting Information. As shown in **Table S1**, Supporting Information, the electron mobilities of PBDB-T:ITIC, PBDB-T:ITIC:FBR (1:0.8:0.2), and PBDB-T:FBR films are 2.15×10^{-4} , 1.47×10^{-4} , and $5.35 \times 10^{-5} \text{ cm}^2 (\text{V S})^{-1}$, respectively. The electron mobility of the PBDB-T:ITIC:FBR ternary film is higher than that of the PBDB-T:FBR binary film, but less than that of the PBDB-T:ITIC binary film. This may be because the electron mobility of FBR is lower than that of ITIC, and therefore, FBR doping in the PBDB-T:ITIC binary film has a negligible effect on the electron mobility of film. Therefore, the improvement of device performance cannot be attributed to the improvement of the mobility within the active layer, but rather to the improved exciton separation and charge collection efficiencies of the ternary system (*vide supra*).

2.4. Device Photovoltaic Properties

Binary and ternary OSCs with an inverted indium tin oxides (ITO)/ZnO/PBDB-T:ITIC:FBR ($1:x:1-x$, w/w/w)/MoO₃/Al

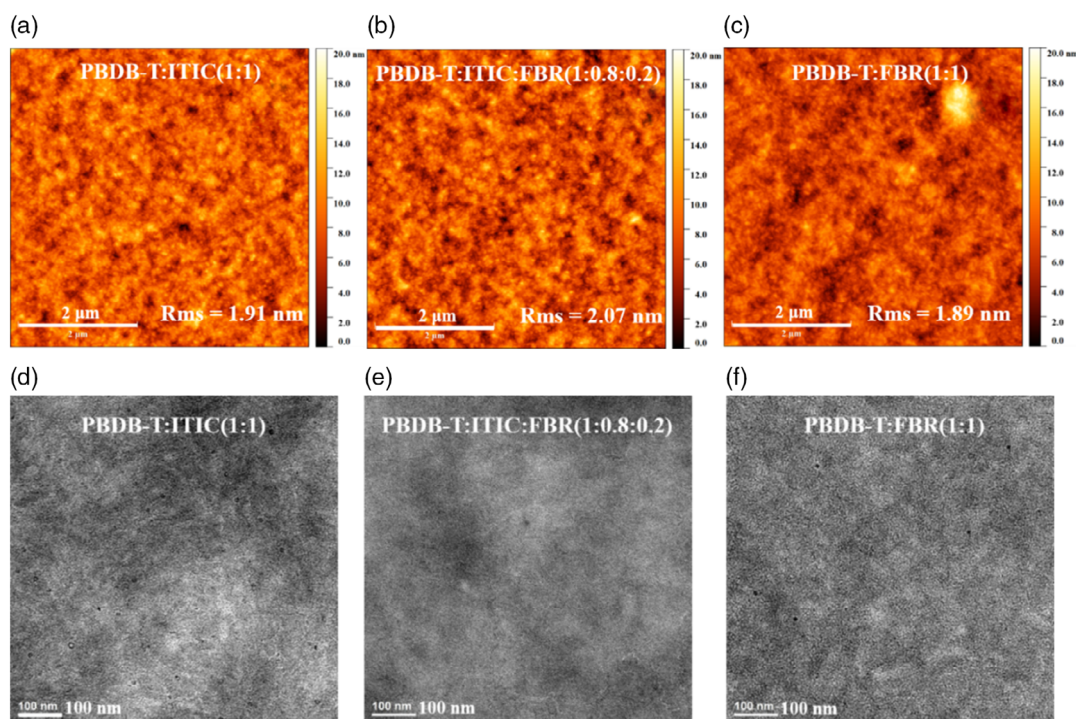


Figure 4. AFM and TEM images of a,d) PBDB-T:ITIC, b,e) PBDB-T:ITIC:FBR, and c,f) PBDB-T:FBR films.

structure were fabricated and tested. **Figure 5a** shows the J - V curves of the best-performing cells, with the detailed photovoltaic parameters summarized in **Table 1**. As demonstrated, the device based on PBDB-T:ITIC exhibits a V_{oc} of 0.88 V, a J_{sc} of 18.07 mA cm^{-2} , and an fill factor (FF) of 62.22%, resulting in an overall PCE of 10.08%, which is similar to that reported in the literature.^[16,23a,b] The binary cell based on PBDB-T:FBR shows a lower PCE of 4.08%, albeit with a surprisingly high V_{oc} of 1.12 V, because the LUMO of FBR is only 0.08 eV higher than that of ITIC, which could be due to the unsatisfying nanomorphology of the blend film, evident from the low FF of 50%. When FBR is doped in a ratio of 20%, the cells show an increased V_{oc} of 0.91 V, a J_{sc} of 18.79 mA cm^{-2} , and an FF of 0.65, yielding an overall PCE of 11.18%, which is over 10% higher than that for the PBDB-T:ITIC binary cell. The EQE spectra show slightly increased photon-to-electric efficiency spanning the 350–500 nm wavelength range (**Figure 5b**), corresponding favorably to the absorption band of FBR, suggesting that J_{sc} enhancement can be caused by the complementary absorption of FBR. The higher V_{oc} of the ternary cell can be ascribed to the high-lying LUMO of FBR, whereas the improved FF could be due to the improved nanomorphology (*vide supra*). The V_{oc} is found to increase monotonically with the increase in the FBR doping ratio, whereas J_{sc} and FF show maxima at a doping ratio of 0.2 (**Figure 5c**). Although we cannot exclude the energy transfer process between FBR and ITIC according to experiment results, the V_{oc} is found to increase monotonically with increasing FBR doping ratios. This suggests that photon-induced charge transfer between PBDB-T and FBR also occurs, and that FBR serves as the electron acceptor in the blend film, as the energy transfer in ternary solar cell systems will not influence the V_{oc} of the cells.^[24a,b]

Consequently, the formation of an ITIC:FBR alloy is proposed, in which the newly formed alloy serves as the acceptor in the blend and PBDB-T serves as the electron donor. The LUMO energy level of the ITIC:FBR alloy lies between those of ITIC and FBR; therefore, the V_{oc} increases with increasing FBR content. Furthermore, the ITIC:FBR alloy improves crystalline structure formation within the blend film (as seen from the GIWAXS results of **Figure 3**), which ultimately improves the FF of devices. It is worth mentioning that the PBDB-T:ITIC:FBR ternary system exhibits high tolerance of the FBR blend ratio. For an FBR content as high as 40%, the PCE of ternary OSCs is 10.87%, which is still higher than that of PBDB-T:ITIC cells. This helps alleviate the strict requirements for component content in actual industrial environments, thereby reducing the difficulty of industrialization. The EQE in **Figure 5b** shows that increasing the FBR content suppresses the contribution of ITIC, which leads to lower J_{sc} values for ternary cells with higher FBR content. This is consistent with the change in the absorption capacity of the ternary blend film (**Figure 1c**).

2.5. Influence of FBR Doping on Charge Generation and Collection Efficiency

To obtain further insights into the influence of FBR doping on the charge generation and collection efficiency within the cells, the photocurrent (J_{ph}) was plotted as a function of the effective voltage (V_{eff}), as shown in **Figure 6a**, where J_{ph} is defined by the difference in the short circuit current density under light illumination (J_L) and in the dark (J_D), and V_{eff} is defined as the difference between the applied voltage (V_a) and the voltage at zero current (V_0). The charge collection probability ($P(E,T)$)

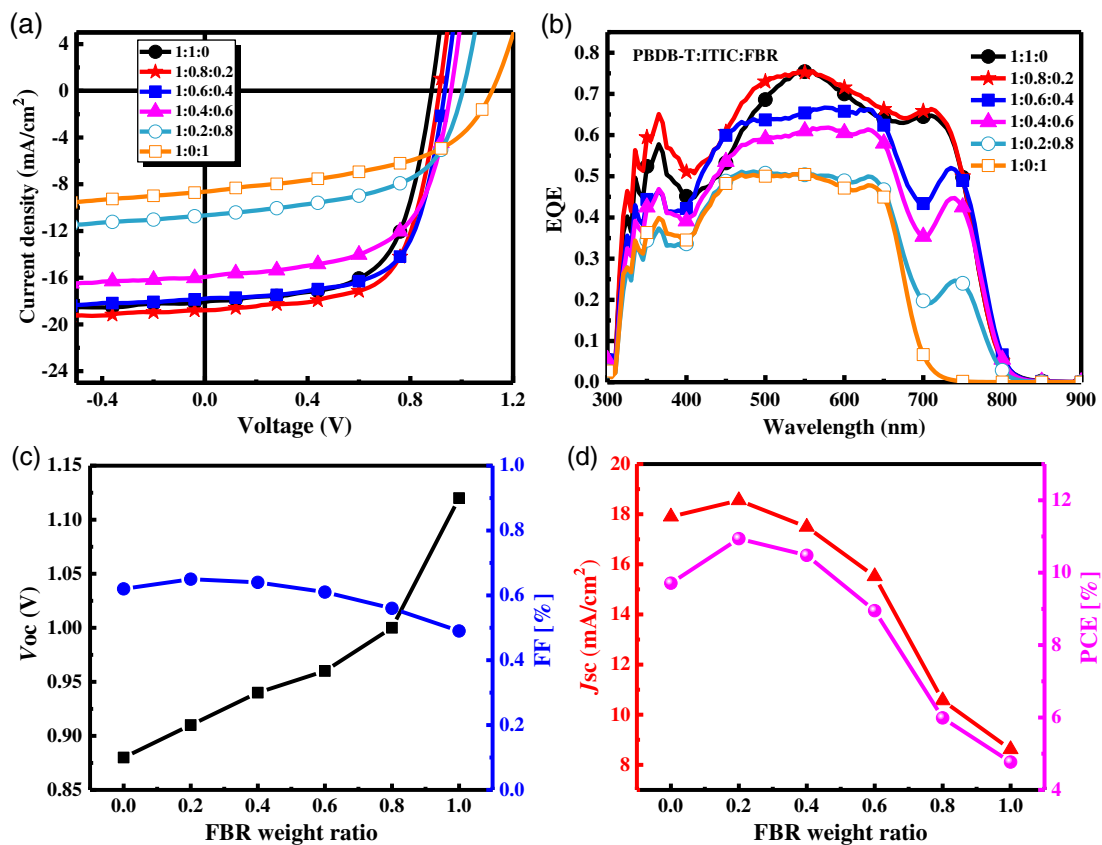


Figure 5. a) J - V curves and b) EQE spectrum of PBDB-T:ITIC:FBR devices. c) V_{oc} and FF and d) J_{sc} and PCE curves of ternary OSCs as a function of increasing FBR weight content.

Table 1. Photovoltaic performance data of PBDB-T:ITIC:FBR devices.

PBDB-T:ITIC:FBR	V_{oc} [V]	J_{sc} [mA cm ⁻²]	FF	PCE [%]	PCE [%] ^{a)}	T_{80} [h] ^{b)}	PCE ³⁵⁰ [%] ^{c)}	PCE [∞] ^{d)}	α^d	τ [h] ^{d)}	β^d
1:1:0	0.88 ± 0.01	17.90 ± 0.10	0.62 ± 0.03	9.71 ± 0.48	10.08	39	52.6	0.49	0.52	160.35	1
1:0.8:0.2	0.91 ± 0.00	18.55 ± 0.18	0.65 ± 0.00	10.94 ± 0.15	11.17	203	71.3	0.69	0.34	339.46	1
1:0.6:0.4	0.94 ± 0.00	17.49 ± 0.22	0.64 ± 0.02	10.48 ± 0.02	10.87	104	66.7	0.61	0.39	252.65	1
1:0.4:0.6	0.96 ± 0.00	15.52 ± 0.39	0.61 ± 0.01	8.95 ± 0.19	9.19	23	48.7	0.24	0.78	250.73	0.42
1:0.2:0.8	1.00 ± 0.00	10.57 ± 0.09	0.56 ± 0.00	5.99 ± 0.03	6.03	7.8	41.2	0.28	0.74	89.68	0.40
1:0:1	1.12 ± 0.00	8.62 ± 0.04	0.49 ± 0.00	4.77 ± 0.02	4.80	2.2	9.12	0.07	0.98	12.67	0.41

^{a)}PCE of the best performing device; ^{b)}Time that reaches 80% of its initial PCE; ^{c)}Ratio of the PCE aged for 350 h to its initial value (in percentage); ^{d)}Numerical simulated results obtained by fitting the normalized PCE decay curves to the exponential stretched decay model (Equation (4)).

corresponding to the short circuit or open circuit condition is estimated as^[25]

$$P(E, T) = J_{ph}/J_{sat} \quad (2)$$

where J_{sat} is the saturated J_{ph} value at $V_{eff} \geq 2$ V. The relevant fitting results as well as the fitting data of all blended devices are listed in Figure S5 and Table S2, Supporting Information. As shown in Figure 6a, the values of $P(E, T)$ relating to the short or open circuit conditions for the PBDB-T:ITIC:FBR (1:0.8:0.2) ternary cell are 95.3% and 78.9%, respectively, which are

higher than those for either of the binary cell at the same condition, indicating that the exciton separation and charge collection efficiencies of the ternary system are improved significantly by introducing FBR as a third component into the PBDB-T:ITIC system; this improvement could be ascribed to the improved nanomorphology of the blended film (*vide infra*).^[26a,b]

In addition, the charge recombination of the binary and ternary solar cells was investigated by testing the variation of J_{sc} and V_{oc} as a function of the incident light intensity (P_{Light}), as shown in Figure 6b,c. The J_{sc} was linearly fitted to P_{Light} according to Equation (4)^[27]

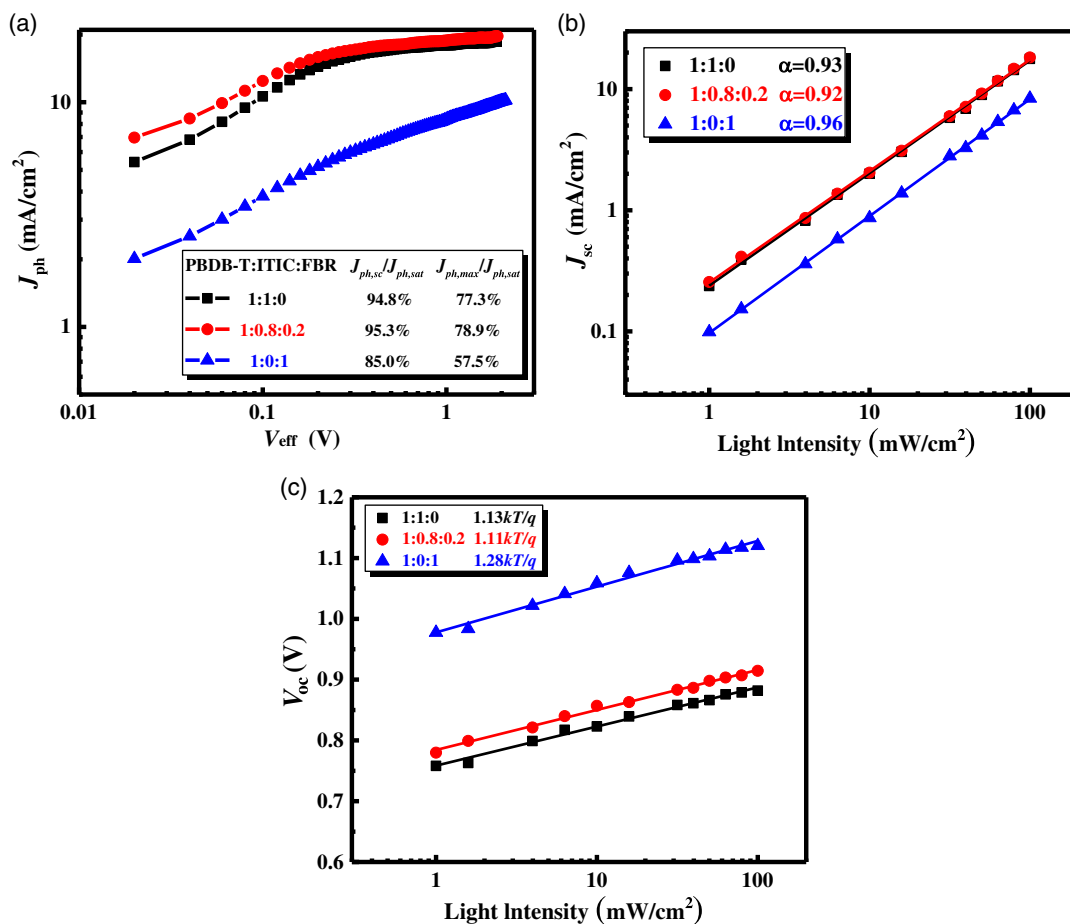


Figure 6. a) J_{ph} - V_{eff} curves of the binary and ternary cells. b, c) Light intensity dependence of J_{sc} and V_{oc} of the cells, respectively.

$$J_{sc} \propto P_{Light}^{\alpha} \quad (3)$$

The exponential factor α was calculated to be 0.93, 0.92, and 0.96 for the PBDB-T:ITIC (1:1), PBDB-T:ITIC:FBR (1:0.8:0.2), and PBDB-T:FBR (1:1) cells, respectively. The similar α values for the ternary and PBDB-T:ITIC cells suggest that the addition of 20% FBR does not increase the extra second-order recombination in the device.^[28] Meanwhile, the dependence of V_{oc} on P_{Light} is plotted in Figure 6b. The slope of the fitting line can be described by $n k_B T/q$, and the n values for PBDB-T:ITIC, PBDB-T:ITIC:FBR, and PBDB-T:FBR were calculated to be 1.13, 1.11, and 1.28, respectively. The small n value for the 20% FBR-doped cell indicates that the monomolecular recombination originates from traps and that defects are reduced by FBR doping, whereas the bimolecular recombination mechanism dominates other device interactions, which can be attributed to the improved morphology of the photoactive layer as a result of FBR doping.

2.6. Stability Characterization

To elucidate the effect of the co-crystallization of FBR with ITIC, the stability of the ternary solar cells under light illumination was

investigated and compared with the binary cells. All devices were tested without encapsulation in a nitrogen glove box ($H_2O < 10$ ppm, $O_2 < 10$ ppm), which ensures the measurement of the intrinsic degradation behavior of the cells. **Figure 7** shows the evolution of the V_{oc} , J_{sc} , FF, and PCE associated with these cells under light illumination. The relevant degradation parameters T_{80} and PCE^{350} are listed in Table 1. These parameters demonstrate that when the PBDB-T:ITIC device is aged for 39 h, it reaches T_{80} . After further aging (350 h), the device performance is only 52.6% compared with that of the pristine device. Moreover, the PBDB-T:FBR cell also shows a very fast performance decay of 2.2 h. The PBDB-T:FBR cell shows poor stability even when stored in the glove box, where a significant reduction in the PCE (about 80%) is observed after 400 h. By contrast, when FBR ($\leq 40\%$) is incorporated into the PBDB-T:ITIC binary blending system, the stability of the ternary blending device is significantly improved, with further improvements observed for its T_{80} (39 h \rightarrow 203 h) and PCE^{350} (52.6% \rightarrow 71.3%) parameters. Surprisingly, increasing the doped amount of FBR further ($\geq 50\%$) leads to the deterioration of the device stability to the extent that it is worse than that of undoped devices. The stability results of the ternary blending device are consistent with the DSC results (Figure 2), primarily because FBR is compatible with the binary blending system, thereby regulating the

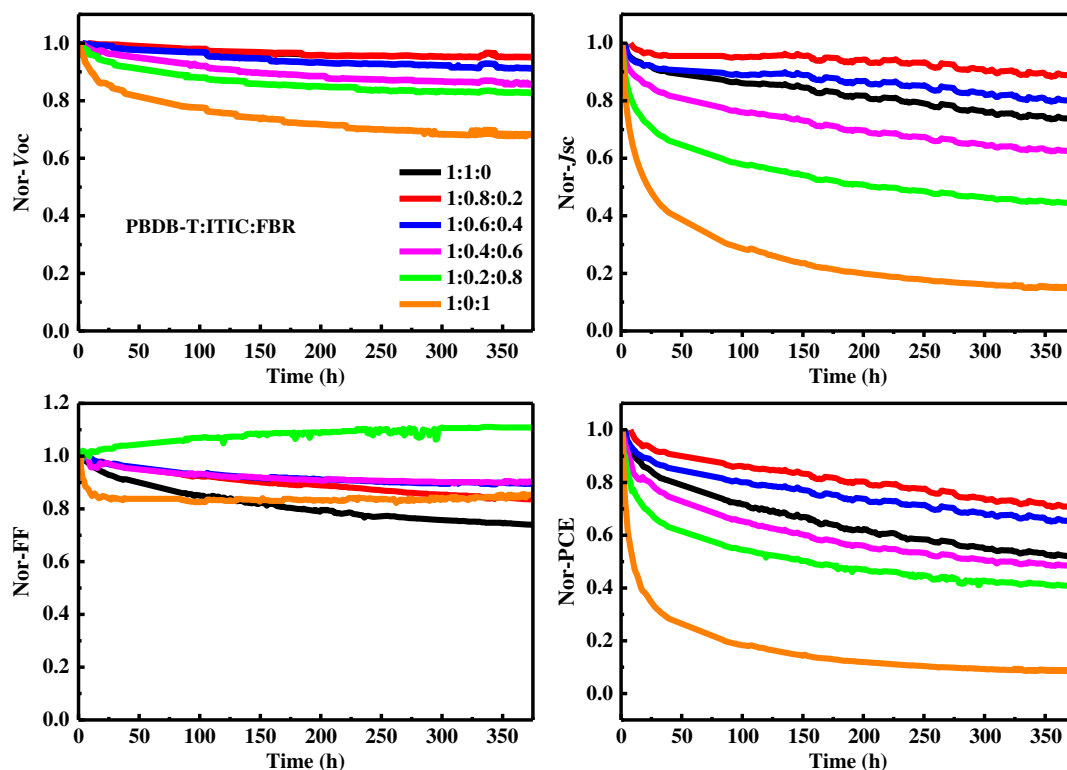


Figure 7. The degradation curves of ternary OSCs.

crystallization of ITIC and promoting the formation of an alloy-like morphology within the active layer of the device, which gives rise to good stability. For lower levels of FBR doping (<50%), stable ITIC:FBR alloy-like crystals are formed, which improves the morphological stability of the active layer, thereby effectively improving the stability of the solar cells. However, excessive FBR doping inhibits the formation of ITIC:FBR alloy-like crystals, which is detrimental to device stability.

To analyze the degradation kinetics of the cells quantitatively, we performed numeric fitting of the PCE decay curves using a stretched exponential decay^[16a,b]

$$PCE(t) = PCE(\infty) + \alpha \times \exp\left(-\frac{t}{\tau}\right)^\beta \quad (4)$$

where τ , α , and $PCE(\infty)$ represent the mean lifetime, pre-exponential factor (degradation amplitude), and the intercept (i.e., the saturated PCE after significant aging), respectively. The stretching exponent β is in the range $0 < \beta \leq 1$, which indicates the complexity of the decay process. The fitting decay curves are shown in Figure S6, Supporting Information, with the corresponding parameters listed in Table 1. It can be observed that the degradation amplitudes (α) are 0.51, 0.39, and 0.98 for the PBDB-T:ITIC (1:1), PBDB-T:ITIC:FBR (1:0.8:0.2), and PBDB-T:FBR (1:1) cells, respectively, clearly indicating that the PBDB-T:ITIC:FBR ternary cell exhibits the slowest degradation behavior. The mean lifetime τ of the cells was fitted as 160.35, 339.46, and 12.67 h for PBDB-T:ITIC (1:1), PBDB-T:ITIC:FBR (1:0.8:0.2), and PBDB-T:FBR (1:1), respectively, again confirming the PBDB-T:ITIC:FBR-based cell as the most stable.

Furthermore, the fitted PCE (∞) predicts the final efficiency of the device after long-term aging, which was found to be close to the measured PCE value after aging for 350 h (PCE^{350} , Table 1)—the PBDB-T:ITIC:FBR (1:0.8:0.2) ternary cell revealed the highest PCE (∞). Together these results confirm that blending the PBDB-T:ITIC cell structure with FBR provides improved device stability, which is ascribed to the formation of an ITIC:FBR alloy as verified via DSC and GIWAXS results.

3. Conclusion

In summary, this work introduces FBR, which has relatively low crystallinity, as a third component into the PBDB-T:ITIC OSC system to achieve the simultaneous improvement of device performance and stability. Consequently, the V_{oc} increases quasi-linearly from 0.88 V for the PBDB-T:ITIC cell to 1.00 V for the PBDB-T:ITIC:FBR (1:0.2:0.8) cell and finally reaches 1.12 V for the PBDB-T:FBR cell. This phenomenon is attributed to the formation of ITIC:FBR alloys in the ternary blend, as confirmed by DSC and GIWAXS results. The optimized cell, with a PBDB-T:ITIC:FBR blend ratio of 1:0.8:0.2, shows the highest PCE (11.17%), demonstrating an increase of more than 10% relative to the PBDB-T:ITIC cell. More importantly, this PBDB-T:ITIC:FBR (1:0.8:0.2) cell also realizes greatly improved device stability, which is also ascribed to the formation of ITIC:FBR alloys. Thus, this study proves that forming electron acceptor alloys via ternary strategies can be an effective way to improve device performance and stability simultaneously.

4. Experiment Section

Materials: PBDB-T ($M_n = 78$ kDa, PDI = 2.1) and ITIC were purchased from Solarmer Materials Inc, Beijing. FBR was purchased from Suna Tech Inc, Suzhou. 1,8-diiodooctane (DIO) was purchased from TCI, Shanghai. Molybdenum oxide (MoO_3) was purchased from Strem Chemicals, Inc., America. Zinc oxide nanoparticles (ZnO) were prepared through the reaction of potassium hydroxide and $\text{Zn}(\text{OAc})_2$ in methanol solvent as reported by Beek et al.^[29] All materials were used as received.

Method for Solar Cell Fabrication: The devices were fabricated from patterned ITO glass (Shenzhen Southern China City Hunan Technology Co. Ltd.). The substrates were sonically cleaned sequentially in detergent, deionized water, acetone, and isopropanol, before being treated in a UV-ozone oven for 30 min. First, filtered ZnO (10 mg mL⁻¹ in methanol) was spin-coated onto the ITO substrates at 2000 rpm for 60 s. Next, the samples were annealed at 130 °C for 10 min on a hot plate. Then, a blend solution of PBDB-T, ITIC, and FBR in chlorobenzene (CB) was spin-coated on the top of the ZnO layer at 2000 rpm for 60 s. The wet PBDB-T:ITIC:FBR blend films were subsequently heated at 140 °C for 30 min. Finally, MoO_3 (10 nm) and Al (100 nm) were vacuum deposited sequentially on the top of the active layer representing the hole-extraction layer and anode, respectively. The substrate measured 2.5×2.5 cm², with an effective photovoltaic area, defined by the geometrical overlap between the bottom cathode and the top anode, of 0.09 cm². For the PBDB-T:ITIC:FBR solar cells, PBDB-T, ITIC, and FBR were mixed in various weight ratios of 1:1- x : x ($x = 0, 0.2, 0.4, 0.6, 0.8, 1$), dissolved in CB with the addition of 0.5% volume ratio of 1,8-DIO, and stirred at 60 °C for 3 h. The total concentration of PBDB-T:ITIC:FBR was 20 mg mL⁻¹.

Test Thin-Film Preparation and Characterization: The model thin films for light illumination tests were prepared by spin-coating the corresponding solution onto the cleaned glass substrates. UV-vis absorption spectra were measured by a Lambda 750 UV/Vis/NIR spectrophotometer (PerkinElmer). AFM images of the films were measured with a Park XE-120 microscope using Cr/Au-coated conducting tips (NSC18, Mikromasch, Tallinn, Estonia). TEM images of the active layers were obtained using a Tecnai G2 F20 S-Twin 200 kV field-emission electron microscope (FEI). The photoactive layers for TEM measurement were prepared by spin-coating the solution onto a cleaned glass substrate, followed by a treatment with hydrofluoric acid vapor in the fume hood. GIWAXS analysis was conducted on an XEUSS small-angle/wide-angle X-ray scattering instrument (Xenocs, France). A Mettler-Toledo differential scanning calorimeter 3+ was used to analyze the thermodynamic behavior of the blended films.

Photovoltaic Performance and Stability Characterizations: The J - V curves of the devices were measured in a N_2 -filled glove box using a Keithley 2400 source meter under illumination by simulated AM 1.5G sunlight (Verasol-2, light emitting diode (LED) 3A Sun simulator, Newport). The EQE spectra were recorded under illumination by a simulated sun operation condition using bias light from a 532 nm solid state laser. The light from a 150 W tungsten halogen lamp (Osram 64610) was used as a probe light and modulated with a mechanical chopper before passing through the monochromator (Zolix, Omni-k300) to select the wavelength. The response was recorded as the voltage by an I - V converter (DNR-IV Converter, Suzhou D&R Instruments) using a lock-in amplifier (Stanford Research Systems SR 830). A calibrated Si cell was used as a reference. The EQE measurement device was placed behind a quartz window in a nitrogen-filled container. Space charged electron mobility (SCLC) was used to test electron mobility of active layers based on three structures (PBDB-T:ITIC, PBDB-T:ITIC:FBR (1:0.8:0.2), and PBDB-T:FBR). The tested devices had an ITO/ZnO/active layer/LiF/Al structure. The final experimental results are shown in Figure S4, Supporting Information, with the electron mobility of the three devices calculated by Equation (1)^[30]

$$J = \frac{9\epsilon_r\epsilon_0\mu_e}{8L^3} V^2 \quad (5)$$

where J is the current density, ϵ_0 is the permittivity of free space (8.85×10^{-12} F m⁻¹), ϵ_r is the dielectric constant of the polymer (assumed

to be 3), μ_e is the space charged electron mobility, V is the voltage difference across the device, and L is the thickness of the active layer.

The long-term stability of un-encapsulated devices was measured using a multi-channel solar cell performance decay test system (PVL-T-G8001M, Suzhou D&R Instruments Co. Ltd.) under a testing condition in accordance with ISOS-L-1. The devices were placed inside a glove box ($\text{H}_2\text{O} < 1$ ppm, $\text{O}_2 < 1$ ppm) and illuminated continuously with white LED light (D&R Light, L-W5300KA-150, Suzhou D&R Instruments). The illumination light intensity was initially set, such that the output short-circuit current (J_{sc}) equaled the J_{sc} measured under standard conditions. The illumination light intensity was monitored by a photodiode (Hamamatsu S1336-8BQ). The J - V curves of devices were checked periodically, and the photovoltaic performance data (V_{oc} , J_{sc} , FF, and PCE) were calculated automatically according to the J - V results. The PCE degradation curves were fitted using the stretched exponential model in the Gnuplot software package (<http://www.gnuplot.info/>).^[31]

Supporting Information

Supporting Information is available from the Wiley Online Library or from the author.

Acknowledgements

The authors would like to acknowledge the financial support from the Ministry of Science and Technology of China (No. 2016YFA0200700), Chinese Academy of Science (No. YJKYYQ20180029, GJHZ2092-019, and CAS-ITRI 2019010), and National Natural Science Foundation of China (61904121). Dr. Q. Luo would like to acknowledge the Youth Innovation Promotion Association of CAS (No. 2019317) for the support.

Conflict of Interest

The authors declare no conflict of interest.

Keywords

non-fullerene acceptors, operation stability of polymer solar cells, organic alloys, polymer solar cells, ternary solar cells

Received: July 13, 2020

Revised: August 17, 2020

Published online: September 6, 2020

- [1] a) L. X. Chen, *ACS Energy Lett.* **2019**, *4*, 2537; b) J. Hou, O. Inganäs, R. H. Friend, F. Gao, *Nat. Mater.* **2018**, *17*, 119; c) J. Ren, Y. Sun, S. Huang, Z. Huai, L. Wang, W. Kong, S. Yang, *Org. Electron.* **2020**, *78*, 105587; d) H. Sun, F. Chen, Z.-K. Chen, *Mater. Today* **2019**, *24*, 94.
- [2] Y. Lin, J. Wang, Z. G. Zhang, H. Bai, Y. Li, D. Zhu, X. Zhan, *Adv. Mater.* **2015**, *27*, 1170.
- [3] Q. Liu, Y. Jiang, K. Jin, J. Qin, J. Xu, W. Li, J. Xiong, J. Liu, Z. Xiao, K. Sun, *Sci. Bull.* **2020**, *65*, 272.
- [4] a) A. Wadsworth, M. Moser, A. Marks, M. S. Little, N. Gasparini, C. J. Brabec, D. Baran, I. McCulloch, *Chem. Soc. Rev.* **2019**, *48*, 1596; b) W. Xu, F. Gao, *Mater. Horizons* **2018**, *5*, 206; c) R. Yu, H. Yao, J. Hou, *Adv. Energy Mater.* **2018**, *8*, 1702814.
- [5] W. Zhao, S. Zhang, J. Hou, *Sci. China Chem.* **2016**, *59*, 1574.
- [6] Y. Zhang, H. Yao, S. Zhang, Y. Qin, J. Zhang, L. Yang, W. Li, Z. Wei, F. Gao, J. Hou, *Sci. China Chem.* **2018**, *61*, 1328.

- [7] W. Zhao, S. Li, H. Yao, S. Zhang, Y. Zhang, B. Yang, J. Hou, *J. Am. Chem. Soc.* **2017**, *139*, 7148.
- [8] H. Jiang, X. Li, Z. Liang, G. Huang, W. Chen, N. Zheng, R. Yang, *J. Mater. Chem. A* **2019**, *7*, 7760.
- [9] P. Q. Bi, C. R. Hall, H. Yin, S. K. So, T. A. Smith, K. P. Ghiggino, X. T. Hao, *J. Phys. Chem. C* **2019**, *123*, 18294.
- [10] Q. An, F. Zhang, W. Gao, Q. Sun, M. Zhang, C. Yang, J. Zhang, *Nano Energy* **2018**, *45*, 177.
- [11] Y. Chen, P. Ye, X. Jia, W. Gu, X. Xu, X. Wu, J. Wu, F. Liu, Z.-G. Zhu, H. Huang, *J. Mater. Chem. A* **2017**, *5*, 19697.
- [12] X. Ma, J. Wang, J. Gao, Z. Hu, C. Xu, X. Zhang, F. Zhang, *Adv. Energy Mater.* **2020**, 2001404.
- [13] Q. An, J. Wang, W. Gao, X. Ma, Z. Hu, J. Gao, C. Xu, M. Hao, X. Zhang, C. Yang, *Sci. Bull.* **2020**, *7*, 538.
- [14] a) B. Wang, Y. Fu, C. Yan, R. Zhang, Q. Yang, Y. Han, Z. Xie, *Front. Chem.* **2018**, *6*, 198; b) P. Bi, T. Xiao, X. Yang, M. Niu, Z. Wen, K. Zhang, W. Qin, S. K. So, G. Lu, X. Hao, *Nano Energy* **2018**, *46*, 81; c) W. Li, D. Yan, F. Liu, T. Russell, C. Zhan, J. Yao, *Sci. China Chem.* **2018**, *61*, 1609; d) Q. Li, Y. Sun, X. Xue, S. Yue, K. Liu, M. Azam, C. Yang, Z. Wang, F. Tan, Y. Chen, *ACS Appl. Mater. Interfaces* **2018**, *11*, 3299.
- [15] W. Huang, S.-Y. Chang, P. Cheng, D. Meng, B. Zhu, S. Nuryyeva, C. Zhu, L. Huo, Z. Wang, M. Wang, *Nano Lett.* **2018**, *18*, 7977.
- [16] L. Xiao, B. He, Q. Hu, L. Maserati, Y. Zhao, B. Yang, M. A. Kolczkowski, C. L. Anderson, N. J. Borys, L. M. Klivansky, *Joule* **2018**, *2*, 2154.
- [17] a) L. Zhang, B. Lin, B. Hu, X. Xu, W. Ma, *Adv. Mater.* **2018**, *30*, 1800343; b) M. B. Upama, N. K. Elumalai, M. A. Mahmud, M. Wright, D. Wang, C. Xu, A. Uddin, *Sol. Energy Mater. Sol. Cells* **2018**, *176*, 109.
- [18] a) S. Li, W. Liu, C. Z. Li, M. Shi, H. Chen, *Small* **2017**, *13*, 1701120; b) Y. Yang, Z.-G. Zhang, H. Bin, S. Chen, L. Gao, L. Xue, C. Yang, Y. Li, *J. Am. Chem. Soc.* **2016**, *138*, 15011.
- [19] L. Yu, D. Qian, S. Marina, F. A. Nugroho, A. Sharma, S. Hultmark, A. I. Hofmann, R. Kroon, J. Benduhn, D.-M. Smilgies, *ACS Appl. Mater. Interfaces* **2019**, *11*, 21766.
- [20] S. Li, L. Ye, W. Zhao, S. Zhang, S. Mukherjee, H. Ade, J. Hou, *Adv. Mater.* **2016**, *28*, 9423.
- [21] R. S. Gurney, W. Li, Y. Yan, D. Liu, A. J. Pearson, T. Wang, *J. Energy Chem.* **2019**, *37*, 148.
- [22] J. Mai, Y. Xiao, G. Zhou, J. Wang, J. Zhu, N. Zhao, X. Zhan, X. Lu, *Adv. Mater.* **2018**, *30*, 1802888.
- [23] a) Z. Fei, F. D. Eisner, X. Jiao, M. Azzouzi, J. A. Röhr, Y. Han, M. Shahid, A. S. Chesman, C. D. Easton, C. R. McNeill, *Adv. Mater.* **2018**, *30*, 1705209; b) S. Park, H. J. Son, *J. Mater. Chem. A* **2019**, *7*, 25830; c) X. Liu, X. Wang, Y. Xiao, Q. Yang, X. Guo, C. Li, *Adv. Energy Mater.* **2020**, *10*, 1903650.
- [24] a) X. Song, N. Gasparini, M. M. Nahid, S. H. K. Paleti, J.-L. Wang, H. Ade, D. Baran, *Joule* **2019**, *3*, 846; b) P. Cheng, J. Wang, Q. Zhang, W. Huang, J. Zhu, R. Wang, S. Y. Chang, P. Sun, L. Meng, H. Zhao, *Adv. Mater.* **2018**, *30*, 1801501.
- [25] R. Peng, Z. Liu, Q. Guan, L. Hong, W. Song, Q. Wei, P. Gao, J. Huang, X. Fan, M. Wang, *J. Mater. Chem. A* **2018**, *6*, 6327.
- [26] a) S. R. Cowan, R. Street, S. Cho, A. Heeger, *Phys. Rev. B* **2011**, *83*, 035205; b) Y. Chen, S. Wang, L. Xue, Z. Zhang, H. Li, L. Wu, Y. Wang, F. Li, F. Zhang, Y. Li, *J. Mater. Chem. A* **2016**, *4*, 19189.
- [27] P. P. Khlyabich, B. Burkhart, B. C. Thompson, *J. Am. Chem. Soc.* **2012**, *134*, 9074.
- [28] A. K. K. Kyaw, D. H. Wang, V. Gupta, W. L. Leong, L. Ke, G. C. Bazan, A. J. Heeger, *ACS Nano* **2013**, *7*, 4569.
- [29] W. J. Beek, M. M. Wienk, M. Kemerink, X. Yang, R. A. Janssen, *J. Phys. Chem. B* **2005**, *109*, 9505.
- [30] X. Guo, N. Zhou, S. J. Lou, J. Smith, D. B. Tice, J. W. Hennek, R. P. Ortiz, J. T. L. Navarrete, S. Li, J. Strzalka, *Nat. Photonics* **2013**, *7*, 825.
- [31] a) M. Berberan-Santos, E. Bodunov, B. Valeur, *Chem. Phys.* **2005**, *315*, 171; b) D. Johnston, *Phys. Rev. B* **2006**, *74*, 184430.